J. Fluid Mech. (2013), *vol.* 720, *pp.* 169–191. © Cambridge University Press 2013
doi:10.1017/jfm.2013.6

Viscous drop in compressional Stokes flow

Michael Zabarankin[1],†, Irina Smagin[2], Olga M. Lavrenteva[2] and Avinoam Nir[2]

[1]Department of Mathematical Sciences, Stevens Institute of Technology, Castle Point on Hudson, Hoboken, NJ 07030, USA

[2]The Wolfson Department of Chemical Engineering, Technion-Israel Institute of Technology, Haifa 32000, Israel

(Received 16 April 2012; revised 6 September 2012; accepted 31 December 2012; first published online 27 February 2013)

The dynamics of the deformation of a drop in axisymmetric compressional viscous flow is addressed through analytical and numerical analyses for a variety of capillary numbers, Ca, and viscosity ratios, λ. For low Ca, the drop is approximated by an oblate spheroid, and an analytical solution is obtained in terms of spheroidal harmonics; whereas, for the case of equal viscosities ($\lambda = 1$), the velocity field within and outside a drop of a given shape admits an integral representation, and steady shapes are found in the form of Chebyshev series. For arbitrary Ca and λ, exact steady shapes are evaluated numerically via an integral equation. The critical Ca, below which a steady drop shape exists, is established for various λ. Remarkably, in contrast to the extensional flow case, critical steady shapes, being flat discs with rounded rims, have similar degrees of deformation ($D \sim 0.75$) for all λ studied. It is also shown that for almost the entire range of Ca and λ, the steady shapes have accurate two-parameter approximations. The validity and implications of spheroidal and two-parameter shape approximations are examined in comparison to the exact steady shapes.

Key words: computational methods, drops, low-Reynolds-number flows

1. Introduction

The flow of two phases, one dispersed in the other, is a fundamental aspect of many processes. Clear examples are mixing, on the one hand, and separation of phases, on the other, as well as many other natural, biological and industrial processes that fall in between these two extremes. Although, in general, the structure of such flows may be complex, when the scale of the inclusions dispersed in the continuous viscous phase is small, and when they are not closely packed, the local flow about an individual inclusion can be linearized so that the undisturbed velocity gradient on this scale is constant.

When the dispersed phase is a fluid, the inclusions are drops and their surfaces can deform. The deformation is an important parameter in the dynamics, break-up and coalescence of the drops. There has been an enormous body of publications concerning the deformation of a drop embedded in a viscous domain and subject to a

† Email address for correspondence: mzabaran@stevens.edu

https://doi.org/10.1017/jfm.2013.6 Published online by Cambridge University Press

slow linear flow, ever since the classical work of Taylor (1934). We shall restrict the review here to those relevant to the current work, i.e. deformation of small drops in a slow viscous flow. In general, a linear flow is of the form $\boldsymbol{u}^{\infty} = \boldsymbol{G}\boldsymbol{x}$, and the constant tensor $\boldsymbol{G}$ contains elements of shear and of extension. When $\boldsymbol{G}$ contains elements only along the diagonal, the extension is either axisymmetric (three-dimensional) or planar (two-dimensional). When the axisymmetric flow along the axis is positive, the flow is referred to as uniaxial or positive extension; whereas when its direction is reversed, it is called biaxial or negative extension. We shall henceforth term these cases 'extensional' and 'compressional' flows, respectively, in view of the expected deformations. The parameters governing the deformation of a drop of radius R are the viscosity ratio $\lambda = \mu^*/\mu$ and the capillary number $Ca = \mu GR/\gamma$. Here μ^* and μ denote the viscosity of the drop and the surrounding fluid, respectively, G is the shear intensity, and γ is the interfacial tension.

Various studies have addressed drop deformations through first- and second-order expansions at small Ca. Cox (1969) and Frankel & Acrivos (1970) used the first-order expansion to analyse small deformations from the initial spherical shape in terms of spherical harmonics (see also Leal 1992), whereas Barthès-Biesel & Acrivos (1973) employed the second-order expansion of $O(Ca^2)$ to obtain finite drop deformation and estimates for critical shapes at burst. Higher-order expansions were reported by Vlahovska, Loewenberg & Blawzdziewicz (2005). Studies of larger deformation have mainly relied on boundary integral equations (BIEs) for Stokes flows (Ladyzhenskaya 1969; Pozrikidis 1992). Rallison & Acrivos (1978) were the first to derive such a BIE for two fluids separated by an interface and applied it to study the deformation of a drop in an extensional flow. They suggested that, following an initial prolate spheroidal shape at low capillary numbers, at higher Ca, the drop attains apparent pointed ends along the symmetry axis. These and many other situations are discussed in a comprehensive review by Stone (1994). Navot (1999) examined the critical conditions at which drops lose the steady shape and modelled it similar to critical phenomena. In a recent work by Zabarankin & Nir (2011), the dynamics and deformation of a drop under extensional flow are revisited and addressed with the approach of generalized analytic functions. An asymptotic consideration of the shapes at the axis of symmetry shows that pointed ends do not exist. Numerous applications and extensions of the pioneering derivation of Rallison & Acrivos (1978) followed, addressing drops and other fluid bodies (e.g. liquid bridges). Examples are the effects of surface-active substances (see e.g. Eggleton & Stebe 1998), the deformation of interacting drops under gravity (Davis 1999), the dynamics and deformation under thermocapillary forcing (Lavrenteva, Berezhnov & Nir 2002), and the dynamics of drops with non-Newtonian rheology (Toose *et al.* 1996), to name just a few.

In contrast to the massive body of publications addressing the deformation of a drop in positive extension, the number of works devoted to the study of the deformation of a single drop experiencing a compressional flow (biaxial extension) is extremely small. Early but limited reports are included in the $O(Ca)$ and $O(Ca^2)$ asymptotic considerations – see Frankel & Acrivos (1970) and Barthès-Biesel & Acrivos (1973), respectively. Kang & Leal (1989) studied numerically the time-dependent deformation of bubbles in axisymmetric compressional flow for Reynolds numbers in the range $0 < Re < 200$, employing the vorticity equation. Unfortunately, this comprehensive and detailed study concentrated on non-zero inertia effects and gave very little information on the creeping flow case. As a follow-up study devoted entirely to a drop in slow viscous compressional flow, Stone & Leal (1989) used the Rallison & Acrivos (1978) BIE to evaluate steady deformations of the drop shape numerically and to address

https://doi.org/10.1017/jfm.2013.6 Published online by Cambridge University Press

the critical condition for loss of stability and dynamics of a drop, over-extended beyond the steady shape, when the forcing flow is relaxed. Recently, Lac & Homsy (2007) used the same BIE to study the deformation of drops, with the force provided by a steady electrical field, and reported subregions with oblate shapes among the deformation patterns. They demonstrated that the deformed drops may have dimples at the axis of symmetry. As yet another study, Bazhlekov, Chesters & van de Vosse (2000) used the BIE to evaluate the deformation of interacting drops in compressional flow and to analyse the drainage of the film from the dimpled gap between the drops.

The results presented by Stone & Leal (1989) were limited to the cases $\lambda = 1$ and $\lambda = 10$. For the steady deformation of such viscous drops under compressional flow, they reported that, for a given Ca, the degree of deformation is larger for $\lambda = 10$ than for $\lambda = 1$. This behaviour resembles that in the case of deformation under extensional flow. However, the pattern of deformation of low-viscosity drops ($\lambda < 1$) has not been addressed. Can low-viscosity drops be flattened to an extreme extent at high Ca in a way similar to predictions for low-viscosity drops in extensional deformation, where a high degree of stable slenderness can be achieved? Another question is for what range of Ca, the shape of deformed drops in compressional flow is close to being oblate spheroidal. The cases of $\lambda = 1$ and $\lambda = 10$ suggest that the range is bounded by 0.1.

This study addresses the dynamics and deformation of a drop subject to a slow viscous compressional flow for a wide range of viscosity ratios, with particular attention to the cases $\lambda \leqslant O(1)$. Specifically, it solves two related problems: the dynamics of a drop of a given shape, with emphasis on spheroidal ones, and the steady shape of a drop under the deforming flow. For the general case of λ, in particular in the range $\lambda \leqslant 1$, the evolution of shapes is analysed numerically based on an integral equation formulation for slow viscous flow (see Toose *et al.* 1996), whereas for $\lambda = 1$ the velocity field within and outside a drop of a given shape has an integral representation similar to that in Zabarankin & Nir (2011), and shapes are obtained in the form of Chebyshev series. For spheroidal shapes, the problems are solved analytically with the approach suggested in Zabarankin & Nir (2011). Some interesting results are that, although the critical capillary number increases dramatically with diminishing drop viscosity, the critical shape is very similar at all λ, having a form of a flat disc with a similar degree of deformation and with a rounded edge at the equator. For practical use, we present a highly accurate two-parameter approximation of the steady deformed drop for all λ and Ca.

Section 2 states the problem. Section 3 presents the integral equation for the velocity field at arbitrary λ when a drop is of a given shape and provides an explicit integral representation for it in the particular case $\lambda = 1$. The special case of spheroidal drops is addressed in § 4. Various solutions and practically useful approximations for steady shapes are presented and discussed in § 5, followed by concluding remarks.

2. Problem formulation

Let a viscous drop of volume V^* be embedded in an immiscible viscous fluid occupying infinite domain V, with S denoting the interface between the phases. The undeformed drop is assumed to be a sphere of radius R, whereas in the absence of the drop, the fluid is subject to a compressional undisturbed flow

$$u_i^\infty = G_{ij} x_j, \tag{2.1}$$

where G_{ij} is the diagonal tensor, with $G_{11} = G_{22} = G$ and $G_{33} = -2G$, with G being the shear rate. Both fluids are assumed incompressible. Let $\boldsymbol{u} = (u_1, u_2, u_3)$ and p

https://doi.org/10.1017/jfm.2013.6 Published online by Cambridge University Press

denote the disturbance velocity and pressure in V, respectively, and let $\boldsymbol{u}^* = (u_1^*, u_2^*, u_3^*)$ and p^* be the actual velocity and pressure in V^*. The flow within and outside the drop satisfies the Stokes equations under the zero-Reynolds-number quasi-stationary approximation,

$$\sigma_{ij,j} = 0, \quad u_{j,j} = 0, \quad \boldsymbol{x} \in V, \tag{2.2a}$$

$$\sigma_{ij,j}^* = 0, \quad u_{j,j}^* = 0, \quad \boldsymbol{x} \in V^*, \tag{2.2b}$$

where σ_{ij} and σ_{ij}^* are the stress tensors in V and V^*, respectively, and are defined by

$$\sigma_{ij} = -p\delta_{ij} + \mu(u_{i,j} + u_{j,i}), \quad \sigma_{ij}^* = -p^*\delta_{ij} + \mu^*(u_{i,j}^* + u_{j,i}^*), \tag{2.3}$$

with δ_{ij} being the unit tensor.

The velocity is continuous at the interface and tends to that of the unperturbed flow at infinity,

$$(u_i + u_i^\infty - u_i^*)|_S = 0, \quad u_i|_\infty = 0, \quad p|_\infty = 0, \tag{2.4}$$

whereas a force balance across the interface, being a generalization of the static Young–Laplace equation (Levich 1962), provides the boundary conditions for the stress

$$(\sigma_{ij} + \sigma_{ij}^\infty - \sigma_{ij}^*)n_j = \gamma\, \mathrm{div}_S \mathfrak{n}\, n_i \quad \text{on } S, \tag{2.5}$$

where $\sigma_{ij}^\infty = \mu(u_{i,j}^\infty + u_{j,i}^\infty)$, $\mathfrak{n} = (n_1, n_2, n_3)$ is the outward normal to the surface S, div_S is the surface divergence operator (see e.g. Aris 1962), and γ is the interfacial tension. At the moving interface between two immiscible fluids, the normal velocity equals the velocity $\mathscr{U}_n$ of the interface S in the direction of $\mathfrak{n}$:

$$u_i^* n_i = \mathscr{U}_n. \tag{2.6}$$

Next we rescale the length with R, the velocity and the pressure and stress fields with GR and μGR, respectively, and use the defined capillary number $Ca = \mu GR/\gamma$ and the viscosity ratio $\lambda = \mu^*/\mu$ for the governing parameters only.

If the drop's shape is given, the velocity and pressure fields are found from the linear (with respect to velocity and pressure) equations (2.2)–(2.5). The kinematic condition (2.6), being nonlinear with respect to the drop's shape as well as the stress balance (2.5), is used to follow the dynamic evolution of the interface and to determine the drop's steady shape, which constitute the main subject of this study.

3. Flow in and around a drop of a given shape

3.1. *Integral equations*

Following Toose *et al.* (1996) and making use of the Green's function for the Stokes equations (see e.g. Ladyzhenskaya 1969; Pozrikidis 1992),

$$J_{ik}(\boldsymbol{x}) = \frac{1}{8\pi}\left(\frac{\delta_{ik}}{\|\boldsymbol{x}\|} + \frac{x_i x_k}{\|\boldsymbol{x}\|^3}\right),$$

one can reduce the problem (2.2)–(2.5) to a system of integral equations

$$u_k^*(\boldsymbol{x}) = u_k^\infty(\boldsymbol{x}) - (\lambda - 1)\int_{V^*} \boldsymbol{\varepsilon}_{ij}(\boldsymbol{y})\partial_j J_{ik}(\boldsymbol{y} - \boldsymbol{x})\, \mathrm{d}V_y$$

$$- \frac{1}{Ca}\oint_S J_{ik}(\boldsymbol{y} - \boldsymbol{x})\, \mathrm{div}_S \mathfrak{n}(\boldsymbol{y})\, n_i(\boldsymbol{y})\, \mathrm{d}S_y, \quad k = 1, 2, 3, \ \boldsymbol{x} \in V^* \cup S, \tag{3.1}$$

https://doi.org/10.1017/jfm.2013.6 Published online by Cambridge University Press

where ∂_i is the partial derivative with respect to y_i, and where, after the use of the divergence theorem and the boundary conditions at S, no integrals over the outer unbounded domain V appear. In (3.1) $\boldsymbol{\varepsilon}$ is the rate-of-strain tensor, with the components $\boldsymbol{\varepsilon}_{ij} = \partial_j u_i^* + \partial_i u_j^*$. Once u_k^* in V^* is found, the right-hand side of (3.1) determines u_k in the ambient fluid for $\boldsymbol{x} \in V$; see Toose *et al.* (1996) and Smagin *et al.* (2011) for details. The formulation (3.1) differs from the BIE, which is commonly used for the simulation of the slow deformation of Newtonian drops and which contains solely surface integrals (see e.g. Rallison & Acrivos 1978; Pozrikidis 1992). It models non-Newtonian drops with a nonlinear constitutive equation, for which involvement of the volume integral is unavoidable. Nevertheless, (3.1) proved to be efficient for Newtonian drops as well (see e.g. Hooper *et al.* 2001), and we adopted the code developed for simulations of viscoplastic drops to the case of viscous drops (Smagin *et al.* 2011). In the case of equal viscosity of the phases, $\lambda = 1$, (3.1) reduces to an explicit expression for the velocity field that coincides with that resulting from the conventional BIE (Rallison & Acrivos 1978; Pozrikidis 1992); see § 3.2. It is well known that, when the viscosity ratio vanishes, direct implementation of the conventional BIE encounters numerical difficulties due to the eigenvalue spectrum in the double-layer term. This issue never arises in the (3.1). Another alternative, though not pursued in this paper, is to employ the Wielandt deflation method (see e.g. Pozrikidis 1992).

Let (r, φ, z) be a cylindrical coordinate system with the basis $(\boldsymbol{e}_r, \boldsymbol{e}_\varphi, \boldsymbol{e}_z)$, and whose z-axis coincides with the x_3-axis. In this case, (2.1) takes the form $\boldsymbol{u}^\infty = G(r\boldsymbol{e}_r - 2z\boldsymbol{e}_z)$, and the problem (2.2)–(2.5) is axially symmetric, where the z-axis is the axis of revolution, so that the velocity and pressure fields are independent of the azimuthal angle φ:

$$\boldsymbol{u} = u_r(r, z)\boldsymbol{e}_r + u_z(r, z)\boldsymbol{e}_z, \quad p = p(r, z), \tag{3.2a}$$

$$\boldsymbol{u}^* = u_r^*(r, z)\boldsymbol{e}_r + u_z^*(r, z)\boldsymbol{e}_z, \quad p^* = p^*(r, z). \tag{3.2b}$$

Let $\mathscr{D}^+$ and $\mathscr{D}^-$ be the interior and exterior of the drop in the meridional rz-plane, respectively, with common boundary ℓ (the cross-section of S). Equation (3.1) can be integrated over the azimuthal angle φ and reduced to the form

$$u_k^*(\boldsymbol{x}) = u_k^\infty(\boldsymbol{x}) - (\lambda - 1)\int_{\mathscr{D}^+} \boldsymbol{\varepsilon}_{ij}(\boldsymbol{y}) W_{ik}^j(\boldsymbol{x}, \boldsymbol{y})\, \mathrm{d}\Omega_y$$

$$- \frac{1}{Ca}\int_\ell M_k^i(\boldsymbol{x}, \boldsymbol{y})\, \mathrm{div}_S \mathfrak{n}(\boldsymbol{y})\, n_i(\boldsymbol{y})\, \mathrm{d}l_y, \quad \boldsymbol{x} \in \mathscr{D}^+ \cup \ell. \tag{3.3}$$

Here $k = r, z$, while $i, j = r, z, \varphi$. The kernels $W_{ik}^j(\boldsymbol{x}, \boldsymbol{y})$ and $M_k^i(\boldsymbol{x}, \boldsymbol{y})$ can be expressed in terms of complete elliptic integrals of the first and second kind (see Toose *et al.* 1996). As in (3.1), once u_k^* in $\mathscr{D}^+$ is found, the right-hand side of (3.3) represents u_k for $\boldsymbol{x} \in \mathscr{D}^-$.

The integral equation (3.3) can be solved iteratively with numerical evaluation of the volume and boundary integrals as follows. The drop interface is represented by N_b boundary elements and is approximated by a cubic spline parametrized by the arclength. Then the components of the normal unit vector and the curvature of the interface entering (3.3) are expressed explicitly in terms of the cubic spline coefficients. The internal domain $\mathscr{D}^+$ is divided into N_v internal quadrilateral cells, and, in order to use standard integration and velocity gradient methods, the cells are mapped onto regular square elements by using quadratic transformations (in terms of local coordinates). The velocity and position vectors of the cells are then approximated by

https://doi.org/10.1017/jfm.2013.6 Published online by Cambridge University Press

the values of interpolating functions at the vertices of each cell. Finally, the boundary integrals are evaluated by the Gauss–Legendre quadrature with the so-called singularity subtraction (Pozrikidis 1992). The outlined numerical procedure is detailed in Smagin *et al.* (2011).

3.2. *Exact integral representations for* $\lambda = 1$

In the case of $\lambda = 1$, the integral equation (3.3) reduces to the exact representation for the velocity field,

$$u_k^*(\boldsymbol{x}) = u_k^\infty(\boldsymbol{x}) - \frac{1}{Ca}\int_\ell M_k^i(\boldsymbol{x},\boldsymbol{y})\,\mathrm{div}_S\mathfrak{n}(\boldsymbol{y})\,n_i(\boldsymbol{y})\,\mathrm{d}l_y \tag{3.4}$$

(see also the formulation in Rallison & Acrivos (1978)).

An alternative integral representation for the velocity field in the meridional rz-plane is given by formula (3.8) (Theorem 3.3) in Zabarankin & Nir (2011), with the changed sign at the term $2z - \mathrm{i}r$:

$$u_z(r,z) + \mathrm{i}u_r(r,z) = \frac{1}{Ca}\int_\ell \mathrm{div}_S\mathfrak{n}(\tau)\,(K_1(\zeta,\tau)\,\mathrm{d}\tau - K_2(\zeta,\tau)\,\overline{\mathrm{d}\tau}), \quad \zeta \in \mathscr{D}^- \cup \ell, \tag{3.5a}$$

$$u_z^*(r,z) + \mathrm{i}u_r^*(r,z) = \mathrm{i}r - 2z + \frac{1}{Ca}\int_\ell \mathrm{div}_S\mathfrak{n}(\tau)\,(K_1(\zeta,\tau)\,\mathrm{d}\tau - K_2(\zeta,\tau)\,\overline{\mathrm{d}\tau}),$$
$$\zeta \in \mathscr{D}^+ \cup \ell, \tag{3.5b}$$

where $\zeta = r + \mathrm{i}z$ and $\tau = r_1 + \mathrm{i}z_1$ with $\mathrm{i} = \sqrt{-1}$, and the kernels K_1 and K_2 are defined by

$$K_1(\zeta,\tau) = \frac{1}{2\pi\mathrm{i}}\frac{z - z_1 - \frac{1}{2}\mathrm{i}(r - r_1)}{\tau - \zeta}\left|\frac{\tau + \overline{\zeta}}{\zeta + \overline{\zeta}}\right|\{(\chi^2(\zeta,\tau) - 1)\mathbb{K}(\chi(\zeta,\tau)) + \mathbb{E}(\chi(\zeta,\tau))\}, \tag{3.6a}$$

$$K_2(\zeta,\tau) = \frac{1}{2\pi\mathrm{i}}\frac{z - z_1 - \frac{1}{2}\mathrm{i}(r + r_1)}{\overline{\tau} + \zeta}\left|\frac{\tau + \overline{\zeta}}{\zeta + \overline{\zeta}}\right|\{\mathbb{K}(\chi(\zeta,\tau)) - \mathbb{E}(\chi(\zeta,\tau))\}, \tag{3.6b}$$

with $\chi^2(\zeta,\tau) = 4r_1 r\,|\tau + \overline{\zeta}|^{-2}$, and where $\mathbb{K}(\chi(\zeta,\tau))$ and $\mathbb{E}(\chi(\zeta,\tau))$ are complete elliptic integrals of the first and second kinds, respectively. In this case, the pressure and vorticity within and outside the drop are represented by formulae (3.9) and (3.10) in Zabarankin & Nir (2011).

Although the integral representations (3.4) and (3.6) are equivalent – with the former being a tensorial formulation of the components and the latter following from the Cauchy integral formula for r-analytic functions (see Zabarankin 2008) – in many cases, (3.5) is more convenient for constructing approximate solutions, for example, when the drop's shape is approximated by a finite functional series (see e.g. Zabarankin & Nir 2011).

4. Analytical solution for oblate spheroidal drops

The velocity field with an embedded oblate spheroidal drop can be found from the integral equation (3.3). However, as in the case of an extensional Stokes flow (see Zabarankin & Nir 2011), an analytical solution has substantial advantages in terms of accuracy and running time.

In the oblate spheroidal coordinates $\xi \in [0,\infty)$ and $\eta \in [0,\pi]$, introduced in the meridional rz-plane by $r = c\cosh\xi\sin\eta$ and $z = c\sinh\xi\cos\eta$, where c is a metric

https://doi.org/10.1017/jfm.2013.6 Published online by Cambridge University Press

parameter, an oblate spheroid is determined by fixing $\xi = s > 0$. In this case,

$$\mathrm{div}_S \mathfrak{n} = n_{i,i} = \frac{\tanh s}{c\sqrt{\sinh^2 s + \cos^2\eta}} + \frac{\sinh s \cosh s}{c\,(\sinh^2 s + \cos^2\eta)^{3/2}}. \tag{4.1}$$

Suppose that the spheroid has the volume of a unit sphere, then $c = (\cosh^2 s \sinh s)^{-1/3}$.

Obtaining an analytical solution for an oblate spheroidal drop in a compressional Stokes flow is similar to that for a prolate spheroidal drop in an extensional Stokes flow presented in § 4 in Zabarankin & Nir (2011), and we provide just the final expressions for the components of the velocity $\boldsymbol{u}$ on ℓ:

$$u_r = \sum_{k=0}^{\infty} A_{2k+1} \mathrm{P}^{(1)}_{2k+1}(\cos\eta), \quad u_z = \sum_{k=0}^{\infty} B_{2k+1} \mathrm{P}_{2k+1}(\cos\eta), \tag{4.2}$$

where $\mathrm{P}^{(k)}_n(\cos\eta)$ is the associated Legendre polynomial of the first kind of order n and rank k (for $k = 0$, the superscript is omitted), and the coefficients A_n and B_n are determined by

$$A_1 = \frac{c\Xi_2^- \cosh s}{2\mathfrak{D}_1}(6(1-\lambda)\sinh s + f_1 + g_1 \tanh s), \quad B_1 = 2A_1 \tanh s, \tag{4.3a}$$

$$A_n = \frac{(-1)^{n+1}}{n(n+1)}(\Theta_n^+ \delta_n^- \Psi_n^- + \Theta_n^- \delta_n^+ \Psi_n^+), \quad n \geqslant 2, \tag{4.3b}$$

$$B_n = (-1)^{n+1}(\Xi_n^+ \delta_n^- \Psi_n^- + \Xi_n^- \delta_n^+ \Psi_n^+), \quad n \geqslant 2, \tag{4.3c}$$

with

$$\Psi_n^{\pm} = \frac{\pm c}{2\mathfrak{D}_n}\left[\frac{(-1)^n}{\lambda^{(1\pm1)/2}}(\Theta_n^{\mp} f_n + \Xi_n^{\mp} g_n) + \left(1 - \frac{1}{\lambda}\right)\delta_n^{\mp}\cosh s\left(\frac{\mathrm{d}\Theta_n^{\pm}}{\mathrm{d}s}\frac{g_n}{n(n+1)} - \Theta_n^{\pm} f_n\right)\right], \tag{4.4}$$

$$\mathfrak{D}_n = \left(1 - \frac{1}{\lambda}\right)\frac{\delta_n^+ \widetilde{\delta}_n^-}{n(n+1)} + (1-\lambda)\frac{\delta_n^- \widetilde{\delta}_n^+}{n(n+1)} - \frac{1}{\cosh^2 s}, \tag{4.5}$$

$$\delta_n^{\pm} = (\sinh^2 s - 1)\Xi_n^{\pm}\Theta_n^{\pm} + \tfrac{1}{2}\sinh(2s)[(\Theta_n^{\pm})^2 - n(n+1)(\Xi_n^{\pm})^2], \tag{4.6}$$

$$\widetilde{\delta}_n^{\pm} = n(n+1)\left(\delta_n^{\pm} + \left(2\Xi_n^{\pm} - \frac{\tanh s}{n(n+1)}\Theta_n^{\pm}\right)\Theta_n^{\pm}\right), \tag{4.7}$$

$$f_n = \frac{2n+1}{2c\,Ca\,n(n+1)}\int_0^{\pi}\left[\mathrm{div}_S \mathfrak{n}\,\frac{\partial r}{\partial \xi}\right]\Big|_{\xi=s} \mathrm{P}^{(1)}_n(\cos\eta)\sin\eta\,\mathrm{d}\eta, \tag{4.8}$$

$$g_n = \frac{2n+1}{2c\,Ca}\int_0^{\pi}\left[\mathrm{div}_S \mathfrak{n}\,\frac{\partial z}{\partial \xi}\right]\Big|_{\xi=s} \mathrm{P}_n(\cos\eta)\sin\eta\,\mathrm{d}\eta, \tag{4.9}$$

and

$$\Xi_n^+ = \mathrm{i}^n \mathrm{P}_n(\mathrm{i}\sinh s), \quad \Theta_n^+ = \mathrm{i}^n \mathrm{P}^{(1)}_n(\mathrm{i}\sinh s), \tag{4.10a}$$

$$\Xi_n^- = \mathrm{i}^{n+1} \mathrm{Q}_n(\mathrm{i}\sinh s), \quad \Theta_n^- = \mathrm{i}^{n+1} \mathrm{Q}^{(1)}_n(\mathrm{i}\sinh s) \tag{4.10b}$$

being the real-valued associated Legendre functions of the first and second kinds, respectively. To determine the velocity fields within and outside the drop, one can

https://doi.org/10.1017/jfm.2013.6 Published online by Cambridge University Press

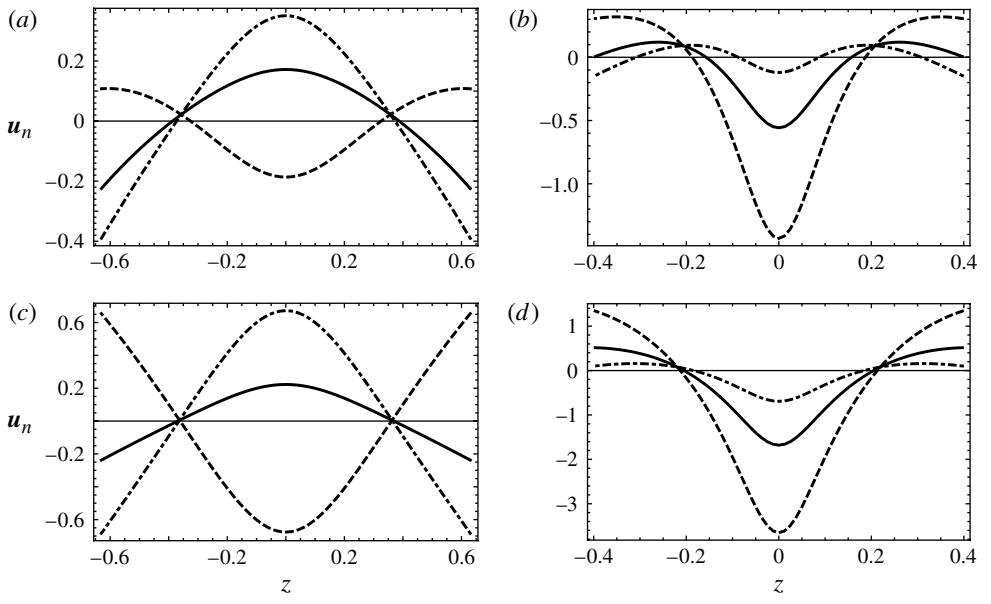


FIGURE 1. Normal velocity at the interface of oblate spheroidal drops as a function of the coordinate z for two spheroid axes ratios κ and two viscosity ratios λ: (*a*) $\kappa = 0.5,\ \lambda = 2$; (*b*) $\kappa = 0.25,\ \lambda = 2$; (*c*) $\kappa = 0.5,\ \lambda = 0.1$; (*d*) $\kappa = 0.25,\ \lambda = 0.1$. Dashed, solid and dashed-dotted lines correspond to $Ca = 0.1$, 0.15 and 0.2, respectively.

introduce stream functions in the oblate spheroidal coordinates based on the boundary values (4.2) (see Payne & Pell 1960; Happel & Brenner 1965).

Figure 1 shows the normal velocity at the boundary of oblate spheroidal drops with short to long axes ratio $\kappa = 0.5$ (figure 1*a*,*c*) and $\kappa = 0.25$ (figure 1*b*,*d*) for various Ca and $\lambda = 2$ and $\lambda = 0.1$. Dashed, solid and dashed-dotted lines correspond to $Ca = 0.1$, 0.15 and 0.2, respectively, with the viscosity ratio $\lambda = 2$ for figure 1(*a*,*b*) and $\lambda = 0.1$ for figure 1(*c*,*d*). For relatively strong flows ($Ca = 0.15$ and 0.2), a spheroid with $\kappa = 0.5$ exhibits a negative normal velocity in the near-z-axis region, while far from the axis, the normal velocity is positive, i.e. the drop expands in the radial direction. However, for spheroids in a weak flow ($Ca = 0.1$), the trend is reversed and the spheroidal shape becomes over-expanded. This behaviour suggests the existence of intermediate cases where the spheroidal shapes are nearly stationary.

In figure 1(*b*,*d*), where the deformation is higher, the velocity at $z = 0$ is negative for all cases, i.e. such shapes are over-extended and tend to shrink. For the cases of relatively low capillary numbers, $Ca = 0.1$ and 0.15 with $\lambda = 0.1$ (dashed-dotted and solid curves in figure 1*d*) and $Ca = 0.1$ with $\lambda = 2$ (dashed-dotted curve in figure 1*b*), the velocity is positive in near-axis regions and the drop shape is anticipated to drift towards a higher axis ratio formation. However, this is not the case for the stronger flow at $Ca = 0.2$. For the cases $Ca = 0.15,\ \lambda = 2$ (solid curve in figure 1*b*) and $Ca = 0.2,\ \lambda = 0.1$ (dashed curve in figure 1*d*), the velocity is nearly zero at the axis and is positive near it, suggesting that the shape flattens or has a dimple in the near-axis regions, thus deviating from spheroidal shape. This is even more evident for the case depicted by a dashed line corresponding to figure 1(*b*) ($\lambda = 2,\ Ca = 0.1$), where the velocity is negative near the axis while being positive at some distance from it.

https://doi.org/10.1017/jfm.2013.6 Published online by Cambridge University Press

5. Steady shapes

The drop has a steady shape when the normal component of the velocity $\boldsymbol{u}^*$ is zero over the surface S of the drop, i.e. when $\mathscr{U}_n = 0$ in (2.6):

$$u_n^* = (u_i + u_i^\infty)n_i = 0 \quad \text{on } S. \tag{5.1}$$

The steady shape S enters the kinematic condition (5.1) nonlinearly and, to the best of our knowledge, has no closed-form representation. In general, finding the steady shape from (5.1) is a computationally intense iterative procedure: each iteration requires solving the integral equation (3.3) and updates the shape in order to decrease the norm of the normal velocity over S, i.e. $\|u_n^*\|_S$. However, in some special cases depending on specified accuracy and on given Ca and λ, practically acceptable solutions can be obtained with substantially less computational effort. For example, for small Ca, steady shapes are close to being spheroidal, in which case, we can use the series-form analytical solution (4.2) for oblate spheroidal drops and can find the optimal spheroid's axes ratio by minimizing $\|u_n^*\|_S$ (single-parameter optimization). Alternatively, for the case of equal viscosities, $\lambda = 1$, one can use the exact integral representations (3.4) and (3.6). Also, if required accuracy is on the scale of 10^{-3}, appropriate steady shapes can be obtained with just two-parameter approximations for almost the entire range of Ca and arbitrary λ. In fact, each case for finding steady shapes assumes two choices: approximation for steady shapes and approach to solving the integral equation (3.3). The two choices are not necessarily dependent and are dictated rather by given values of Ca and λ and by the specified shape accuracy. We will discuss the following four approximations (so-called 'practical solutions') for the steady shape.

(*a*) *Pointwise steady shapes.* For arbitrary Ca and λ (general case), steady shapes are found pointwisely by the iterative procedure described in § 5.1 and will be referred to as pointwise steady shapes.

(*b*) *Spheroidal 'steady' shapes (single-parameter approximation).* The cross-section of the spheroidal 'steady' shape in the rz-plane can be determined by

$$r(t) = a\cos t, \quad z(t) = b\sin t, \quad t \in [-\pi/2, \pi/2], \tag{5.2}$$

where the axes a and b satisfy the volume constraint $\pi a^2 b = 4\pi/3$, and thus this approximation has a single free parameter.

(*c*) *Two-parameter 'steady' shapes.* As a generalization of the spheroidal approximation, the cross-section of the steady shape can be represented by a curve

$$r(t) = a\,(1 - t^2)^\alpha, \quad z(t) = bt, \quad t \in [-1, 1], \tag{5.3}$$

where a, b and α are parameters. For $\alpha = 1/2$, this curve defines the cross-section of an oblate spheroid. Because of the volume constraint, a, b and α are related. Instead, it is convenient to use the ratio $\kappa = b/a$ and α, so that the shape is parametrized by two free parameters κ and α:

$$r(t) = \sqrt[3]{\frac{4\Gamma[\frac{3}{2} + 2\alpha]}{3\sqrt{\pi}\kappa\,\Gamma[1 + 2\alpha]}}\,(1 - t^2)^\alpha, \quad z(t) = \sqrt[3]{\frac{4\kappa^2\Gamma[\frac{3}{2} + 2\alpha]}{3\sqrt{\pi}\,\Gamma[1 + 2\alpha]}}\,t, \quad t \in [-1, 1], \tag{5.4}$$

and satisfies the volume constraint identically. The parameters κ and α have a clear meaning: κ is the axes ratio, whereas α specifies the degree of the shape's ellipticity (the closer α is to $1/2$, the more elliptic the shape is).

https://doi.org/10.1017/jfm.2013.6 Published online by Cambridge University Press

(*d*) *Chebyshev-series steady shapes (multi-parameter approximation).* In the meridional rz-plane, the shape of the drop $\zeta = r + \mathrm{i}z$ can be approximated by a series of Chebyshev polynomials $\mathrm{T}_j(t)$ of the first kind with real-valued coefficients $a_0, \ldots, a_{n_1}, \ b_0, \ldots, b_{n_2}$:

$$\zeta(t) = \nu\left(\cos(\pi t/2)\sum_{j=0}^{n_1} a_j \mathrm{T}_{2j}(t) + \mathrm{i}\sin(\pi t/2)\sum_{j=0}^{n_2} b_j \mathrm{T}_{2j}(t)\right), \quad t \in [-1, 1], \tag{5.5}$$

where the multiplier ν is chosen to satisfy the volume constraint $\pi\int_{-1}^{1} r^2 z' \,\mathrm{d}t = 4\pi/3$ (see Zabarankin & Nir 2011).

Note that the shapes in (*a*) and (*d*) can make the error $\|u_n^*\|_S$ potentially as small as specified, provided that the number of points in (*a*) and n_1 and n_2 in (*d*) are unconstrained; whereas the shapes with *a priori* limited number of parameters as in (*b*) and (*c*) can only reduce the error to some extent. This explains why in (*b*) and (*c*), 'steady' is quoted. Also, with fixed ν, the approximation (5.5) depends on a_j and b_j linearly, which is crucial in finding steady shapes with relatively simple Algorithm 1 in Zabarankin & Nir (2011). For example, (5.5) can be improved by introducing the multiplier $(1-t^2)^{\alpha}$ as in (5.4); however, in this case, simultaneously finding α, a_j and b_j requires a more complex optimization procedure. In fact, this is the case in (5.4), but since (5.4) has only two parameters α and κ, the procedure is not yet computationally intense. Section 5.4 shows that (5.4) has a fairly small error for the entire range of investigated Ca and λ, and, with only two parameters to determine, it provides a good balance between desired accuracy and required computational effort, which makes it attractive for practical use. However, (5.4) is an *ad hoc* approximation, which may not be appropriate for a different axisymmetric flow field, i.e. in a different drop evolution problem, it should again be tested against exact shapes.

Now we proceed with discussing the validity and implications of each steady-shape approximation.

5.1. *General case: pointwise steady shapes*

The steady deformation patterns are established by the following iterative procedure: for a given shape, solve the corresponding integral equation, evaluate the normal velocity on S, perform a small deformation and proceed in a quasi-steady manner while keeping the volume constant during this progress. The procedure starts with a spherical shape and unperturbed velocity for the initial approximation at $t = 0$ and stops when $\|u_n^*\|_S \leqslant \epsilon$, where $\epsilon = 10^{-3}$, 10^{-4} and 10^{-5} is the error tolerance for $\lambda \leqslant 2$, $\lambda = 10$ and $\lambda = 100$, respectively. Consequently, the procedure uses the converged solution at the previous time step as the initial approximation for the next time step and proceeds until the stopping criterion is met. For viscosity ratio in the range $0 \leqslant \lambda \leqslant 2$, the procedure solves (3.3), whereas for $2 \leqslant \lambda \leqslant 100$, it relies on the BIE of Rallison & Acrivos (1978). As a verification, solutions of both integral equations for $\lambda = 1$ and $\lambda = 2$ are found to coincide with sufficient degree of accuracy. Pointwise steady shapes are obtained with the interface line ℓ divided into 100 intervals, and their accuracy is checked by running the procedure for 200 and 400 intervals. (The symmetry of the flow with respect to the z-axis implies that all computations can be conducted for the half of ℓ ($z \geqslant 0$).) Specifically, the deviation in the steady shapes computed with 100 and 400 intervals is of $O(10^{-4})$, and no difference in the critical capillary number Ca_{cr} is detected. Also, the increase of the number of intervals from 100 to 400 allows one to improve (decrease) the error

https://doi.org/10.1017/jfm.2013.6 Published online by Cambridge University Press

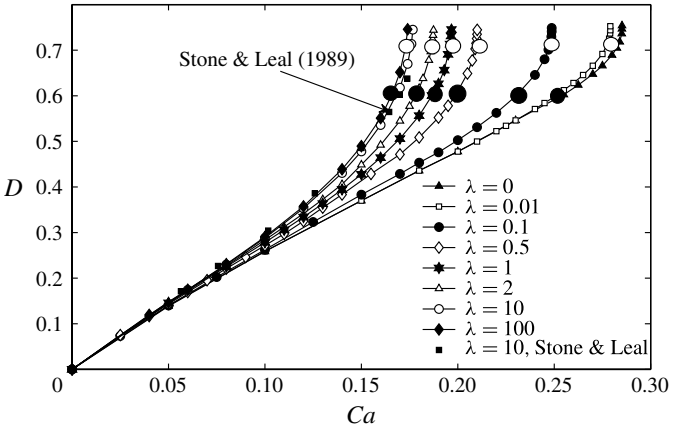


FIGURE 2. Deformation parameter versus capillary number for various viscosity ratios.

tolerance ϵ by two orders of magnitude when Ca is far from Ca_{cr} and by an order of magnitude when Ca is near Ca_{cr}.

The results are summarized in figures 2 and 3. Figure 2 shows the Taylor deformation parameter $D = (1-\kappa)/(1+\kappa)$ as a function of Ca for various viscosity ratios, where κ is the ratio of the half-thickness of the compressed drop at the axis of symmetry to its radius at $z = 0$. It also includes the case $\lambda = 10$ reported earlier by Stone & Leal (1989). Figure 3 depicts pointwise steady shapes for a variety of values of Ca and λ, where in particular the dashed and dashed-dotted lines are the shapes with $\kappa \sim 1/6$ and $\kappa \sim 1/4$, respectively, that correspond to the large white and black circles in figure 2.

It is interesting to compare these results to the pattern of deformation of a drop in a positive (uniaxial) extension, and highlight the similarities and the differences. For $Ca < 0.1$, the drop deformation is only mildly dependent on the viscosity ratio. This conforms to the first-order perturbation analysis for a drop deforming in any linear flow field (see e.g. Leal 1992), where

$$D = \frac{3}{16}\frac{19\lambda + 16}{\lambda + 1} Ca + O(Ca^2). \tag{5.6}$$

The slopes of the deformation curves in figure 2 are almost constant (they vary less than 5 % over the range $0 < Ca < 0.1$ for each value of λ) and change monotonically from 3.0 for $\lambda = 0$ to 3.56 for $\lambda = 100$. Figure 3 shows that, for $Ca < 0.1$ and in all cases of λ, the deformed drop shapes are close to being oblate spheroidal. As Ca exceeds 0.1 and nonlinear effects become non-negligible, the drop shapes become flatter and lose spheroidal similarity (see also § 5.4).

With a further increase of Ca, the drops reach a relatively high deformation and resemble a flat disc with rounded rim. The iterative procedure now becomes slowly convergent. For each λ, there is a critical capillary number, Ca_{cr}, and an associated critical deformation, D_{cr}, beyond which the deformation proceeds without bound, and thus no steady shape exists. The slopes of the deformation curves become extremely steep (see figure 2) and a direct estimation of Ca_{cr} or D_{cr} becomes very expensive with ever increasing errors. Yet, surprisingly, and in contrast to what is known for the deformation of drops in extensional flow, where low-viscosity drops can achieve high elongation and become very slender, the degree of deformation of the drops

https://doi.org/10.1017/jfm.2013.6 Published online by Cambridge University Press

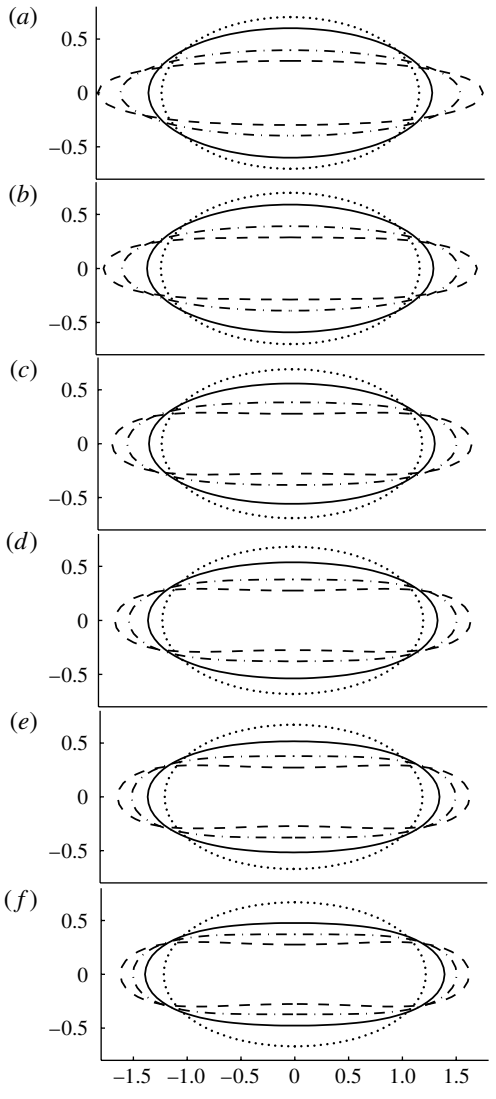


FIGURE 3. Pointwise steady shapes of a drop in compressional flow for various capillary numbers Ca and viscosity ratios (*a*) $\lambda = 0.01$, (*b*) $\lambda = 0.1$, (*c*) $\lambda = 0.5$, (*d*) $\lambda = 1$, (*e*) $\lambda = 2$ and (*f*) $\lambda = 100$. Dotted and solid lines correspond to $Ca = 0.1$ and 0.15, respectively, throughout. Dashed-dotted lines: (*a*) $Ca = 0.25$, (*b*) 0.23, (*c*) 0.199, (*d*) 0.187, (*e*) 0.178 and (*f*) 0.166. Dashed lines: (*a*) $Ca = 0.278$, (*b*) 0.248, (*c*) 0.21, (*d*) 0.196, (*e*) 0.187 and (*f*) 0.173.

in compressional flow is very limited and is similar at all examined viscosity ratios, including the case $\lambda = 0$. Note that, since D_{cr} is very similar for $\lambda = O(1)$ and for $\lambda \ll 1$, and since the shape's rim is more rounded for $\lambda = O(1)$ than for $\lambda \ll 1$, the preservation of the volume implies that, near the critical state, the drop becomes thinner as the viscosity ratio increases (see also figure 2). Furthermore, the near critical shapes are slightly dimpled at the z-axis (axis of revolution) in all the cases of $\lambda = O(1)$. Stone & Leal (1989) observed the same phenomenon for $\lambda = 10$ and $\lambda = 1$,

https://doi.org/10.1017/jfm.2013.6 Published online by Cambridge University Press

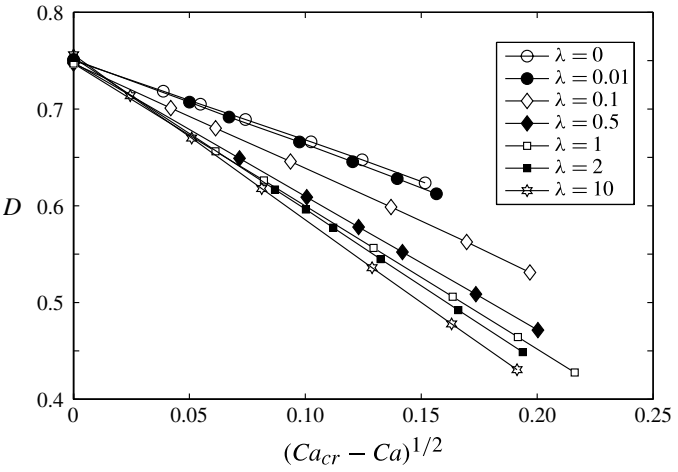


FIGURE 4. Deformation parameter versus $(Ca_{cr} - Ca)^{1/2}$ in the near-critical region for various viscosity ratios.

but did not rule out that such an indentation could result from the accumulating error in the numerical procedure. However, the dimples appeared in the pointwise steady shapes, obtained by the integral equation (3.3) different from the one used by Stone and Leal, and also in the Chebyshev-series steady shapes that follow from an entirely different procedure (see § 5.2). Thus, it seems very probable that steady shapes with slightly dimpled midsection do appear for $\lambda \geqslant O(1)$ just prior to the loss of stability at $Ca \sim Ca_{cr}$. This is further verified by following the evolution that starts from the steady state at $\lambda = 1$, $Ca = 0.196$ and for which Ca is reduced to 0.195 at $t = 0$. With the velocity field represented by (3.4), the shape evolves smoothly to the one obtained for $Ca = 0.195$ from below.

Next we estimate Ca_{cr} and D_{cr} for various λ with the argument of Navot (1999), who considered the transitions from stable drop shapes to unstable ones as critical phenomena. For the compressional flow, the argument yields a linear relation between D and $(Ca_{cr} - Ca)^{1/2}$ shown in figure 4 for various λ, where the points on the ordinate are extrapolations of these linear relations and are in fact estimates of D_{cr}. These results are summarized in table 1. (As a matter of precaution, because of degrading accuracy near the critical points, the extrapolation does not use the last four points on each curve in figure 2, which, in fact, correspond to the disputed dimpled shapes.)

Figure 5 plots Ca_{cr} versus λ on linear (figure 5*a*) and logarithmic (figure 5*b*) scales to emphasize the dramatic increase in the critical capillary number with the decrease of λ. This is in sharp contrast to the practically constant critical deformation $D_{cr} \sim 0.75$ as a function of λ. This behaviour, though hinted at by the limited results of Stone & Leal (1989), is shown here clearly also for diminishing viscosity ratios and is rather unexpected.

5.2. *Chebyshev-series steady shapes,* $\lambda = 1$

In the case of equal viscosity, i.e. $\lambda = 1$, the velocity fields have explicit equivalent integral representations (3.4) and (3.6). If the steady shape is approximated by the Chebyshev series (5.5), then for each Ca, the coefficients in (5.5) can be found by minimizing the norm $\|u_n^*\|_S$ with Algorithm 1 in Zabarankin & Nir (2011). In fact, the Chebyshev series (5.5) can be used for finding steady shapes for arbitrary viscosity

https://doi.org/10.1017/jfm.2013.6 Published online by Cambridge University Press

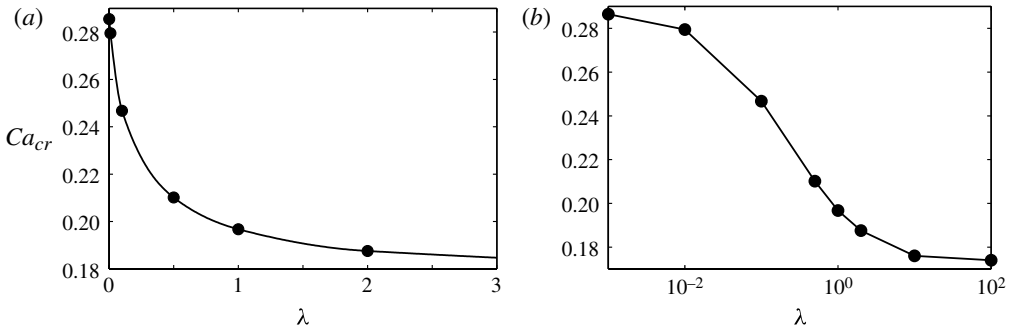


FIGURE 5. Critical capillary number versus viscosity ratio on (*a*) linear scale and (*b*) logarithmic scale.

λ	0	0.01	0.1	0.5	1	2	10	100
Ca_{cr}	0.2855	0.2795	0.24875	0.21013	0.19675	0.18755	0.176	0.174
D_{cr}	0.7502	0.751	0.745	0.748	0.747	0.753	0.753	0.753

TABLE 1. Critical capillary numbers and deformation parameters.

ratios, but this general case requires solving the integral equation (3.3) and becomes computationally intense – see, for example, Zabarankin & Molyboha (2011) for a similar iterative procedure, where (5.5) approximates minimum-drag shapes for solid bodies translating in a viscous incompressible fluid under non-zero Reynolds number.

Figure 6 compares the Chebyshev-series steady shapes (thin solid lines) with the pointwise steady shapes (thick dotted lines) for $\lambda = 1$ and $Ca = 0.1$, 0.15 and 0.196. It shows that the corresponding shapes, though being obtained by different iterative procedures, agree to a high degree of accuracy. Table 2 presents the corresponding Chebyshev-series coefficients and provides an additional quantitative insight. Namely, for $Ca = 0.1$, all coefficients except a_0 and b_0 are sufficiently small, which confirms that the steady shape is very close to being oblate spheroidal, whereas for $Ca = 0.15$, a_1 and b_1 are increased by an order of magnitude, thereby indicating the deviation from a spheroidal shape. Then, for $Ca = 0.196$, the high-order coefficients are non-negligible, and $\|u_n^*\|_S$, being considerably increased, becomes almost insensitive to the number of coefficients. This indicates that Ca approaches its critical value. Indeed, the shape now is flat, far from resembling a spheroid, and has a dimple centred at the z-axis (axis of symmetry), which precedes the loss of stability. In addition, the fact that $\|u_n^*\|_S$ does not vanish for $Ca = 0.2$ confirms that critical Ca is below 0.2.

Figure 7 presents streamlines inside and outside the drop in the rz-plane for $\lambda = 1$ at various degrees of deformation, $Ca = 0.1$ (figure 7*a*), 0.15 (figure 7*b*) and 0.19 (figure 7*c*): the shape in figure 7(*a*) resembles an oblate spheroid, the shape in figure 7(*b*) deviates slightly from a spheroid, and the flat shape in figure 7(*c*) occurs just before the loss of stability but still before the appearance of a dimple. In all three cases, the flow patterns are very similar, with no internal separation. Also, inside the drop, the streamlines are ever squeezed as the flow approaches the surface and the focal point of the vortex is shifted towards the equator as a result of the increasing surface velocity with the coordinate r.

https://doi.org/10.1017/jfm.2013.6 Published online by Cambridge University Press

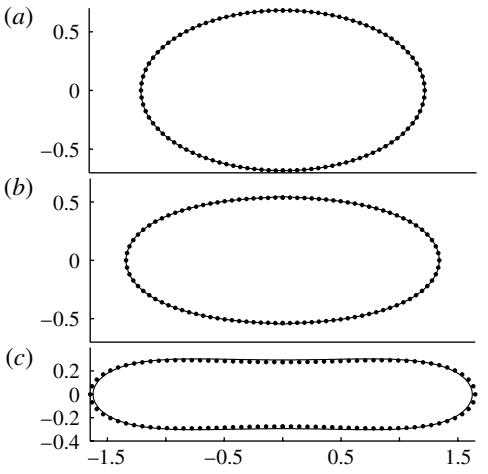


FIGURE 6. The cross-section of the pointwise steady shape (dotted lines) and Chebyshev-series steady shape (solid lines) in the rz-plane for $\lambda = 1$ and (*a*) $Ca = 0.1$, (*b*) $Ca = 0.15$ and (*c*) $Ca = 0.196$.

Ca	0.1	0.15	0.19	0.196
v	1.122 038	0.666 090	1.220 737	1.328 025
a_0	1.079 6872	1.905 779	1.135 884	1.162 492
a_1	2.416×10^{-3}	−0.171 10	−0.019 98	0.005 616
a_2	-8.73×10^{-4}	−0.056 71	0.008 570	0.044 062
a_3	-1.09×10^{-5}	7.399×10^{-3}	−0.017 39	−0.071 54
a_4	1.878×10^{-5}	4.876×10^{-7}	−0.000 67	0.000 2270
a_5	6.489×10^{-7}	-4.04×10^{-4}	−0.001 33	−0.0024
a_6	0	0	0	0.001 352
a_7	0	0	0	0.000 040
b_0	0.609 555	0.825 527	0.325 551	0.294 863
b_1	-2.89×10^{-3}	−0.013 07	−0.078 71	−0.108 04
b_2	9.135×10^{-4}	1.020×10^{-3}	0.030 110	0.044 611
b_3	-9.73×10^{-5}	5.152×10^{-3}	−0.007 03	−0.013 12
b_4	6.305×10^{-6}	4.034×10^{-4}	0.001 979	0.004 760
b_5	2.892×10^{-7}	7.098×10^{-5}	−0.000 46	−0.001 65
b_6	0	0	0	0.000 050
b_7	0	0	0	−0.000 11
$\|u_n^*\|_S$	1.42203×10^{-5}	3.0711×10^{-5}	1.2×10^{-3}	2×10^{-3}

TABLE 2. Coefficients for the Chebyshev-series steady shape (5.5) for $\lambda = 1$.

5.3. *Spheroidal 'steady' shape*

In various two-phase flow problems, actual drop shapes are approximated by spheroids. This approximation often yields closed-form analytical solutions for the velocity, pressure and vorticity fields inside and outside drops, which are computationally efficient, but their applicability may quickly diminish with an increase of the capillary number. Recently, Zabarankin & Nir (2011) showed that prolate spheroidal shapes provide a good approximation to the droplet dynamics in an axisymmetric extensional

https://doi.org/10.1017/jfm.2013.6 Published online by Cambridge University Press

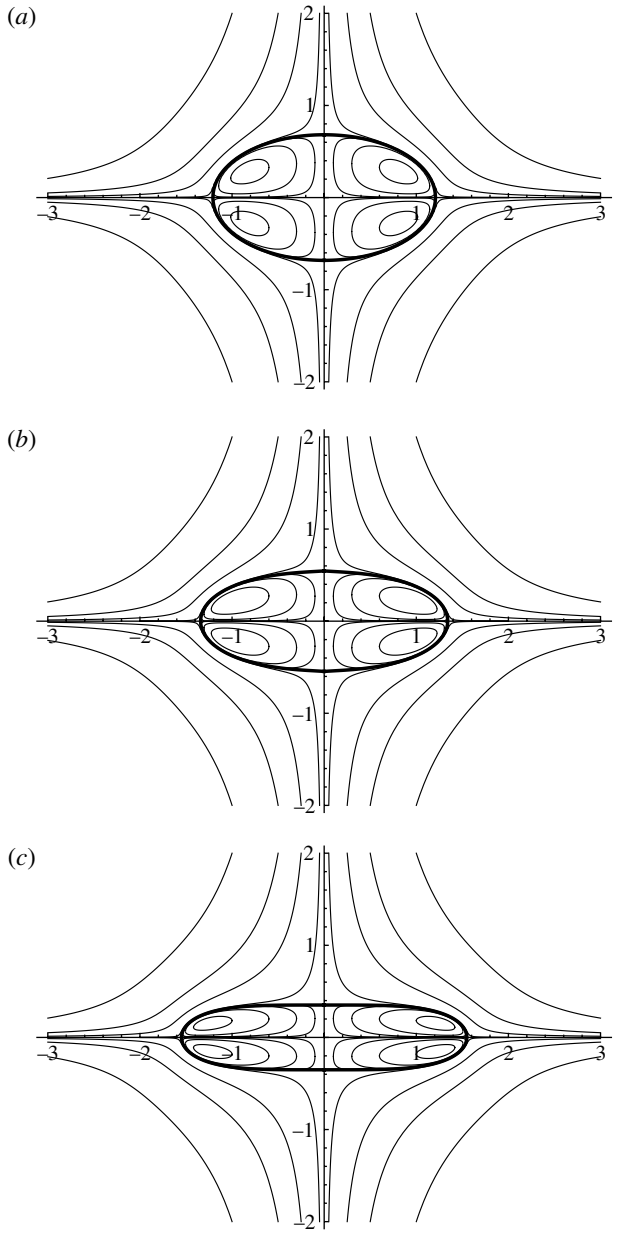


FIGURE 7. Streamlines for the steady shape in the rz-plane for $\lambda = 1$ and (a) $Ca = 0.1$, (b) $Ca = 0.15$ and (c) $Ca = 0.19$.

flow, at least in some vicinity of $\lambda = 1$ for all Ca. This section investigates the range of Ca for which the compressional flow admits spheroidal steady shapes.

For given Ca and λ, a 'steady' spheroidal drop is found by minimizing the norm $\|(u_i + u_i^\infty)n_i\|$ with respect to the shape parameter $\xi = s$, where $\boldsymbol{u}$ on the boundary is determined by (4.2). Figure 8 compares the 'steady' oblate spheroids (diamonds) with corresponding pointwise steady shapes (dots) and two-parameter 'steady' shapes (solid

https://doi.org/10.1017/jfm.2013.6 Published online by Cambridge University Press

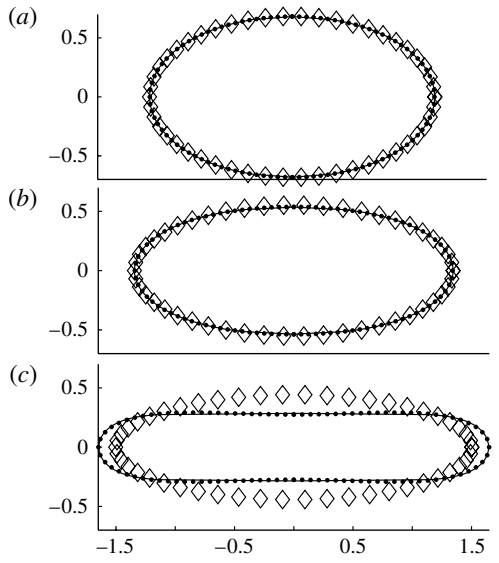


FIGURE 8. Two-parameter 'steady' shape (solid line), pointwise steady shape (dots) and 'steady' spheroids (diamonds) for $\lambda = 1$ and (*a*) $Ca = 0.1$, (*b*) $Ca = 0.15$ and (*c*) $Ca = 0.196$.

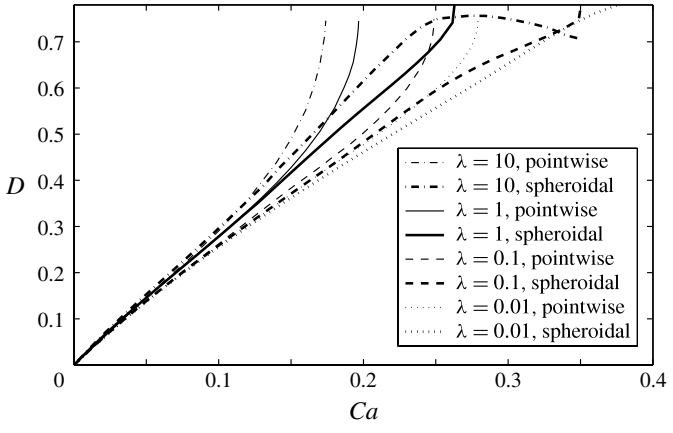


FIGURE 9. Deformation parameter D of the 'steady' oblate spheroid (thick curves) versus Ca for $\lambda = 0.01$ (dotted), 0.1 (dashed), 1 (solid) and 10 (dashed-dotted). Thin curves correspond to the pointwise steady shape.

lines, see § 5.4) for $\lambda = 1$ and $Ca = 0.1$, 0.15 and 0.196. It shows that the deformed drop is nearly a perfect spheroid up to $Ca = 0.1$, then deviates slightly from a spheroid at $Ca = 0.15$, and is apparently far from being spheroidal for higher Ca as it becomes more and more flat at the axis of symmetry.

Figure 9 compares the deformation parameters D for the 'steady' oblate spheroids (thick lines) and pointwise steady shapes (thin lines, see also figure 2) as functions of Ca for $\lambda = 0.01$, 0.1, 1, 10 and 100. It shows that the corresponding deformation curves are indistinguishable for $Ca \leqslant 0.1$, are fairly close for $Ca \leqslant 0.15$, and differ

https://doi.org/10.1017/jfm.2013.6 Published online by Cambridge University Press

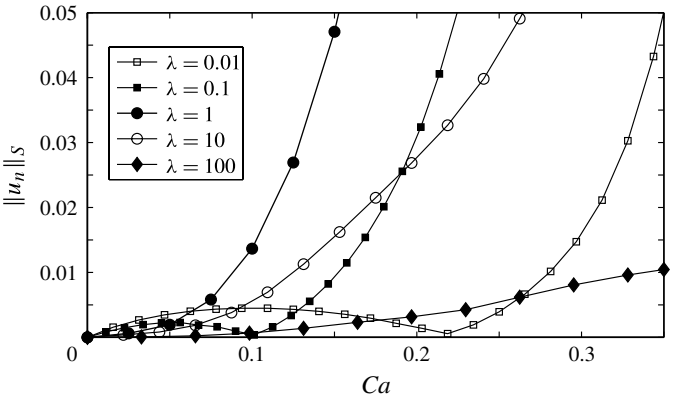


FIGURE 10. Kinematic condition error $\|u_n^*\|_S$ for 'steady' spheroids as a function of Ca for various viscosity ratios.

significantly as Ca increases further. 'Steady' spheroids do not have a clearly defined notion of critical Ca, since they never satisfy the kinematic condition exactly. In this case, defining a critical Ca is just a matter of specifying a threshold for the kinematic condition error, e.g. 0.005 or 0.01 (see figure 10).

The conclusion from the above comparison is that the drop, deformed in a compressional flow, can be simulated as an oblate spheroid only for the range $0 < Ca < 0.15$, which, as is evident from figure 2, conforms to the range where the problem is also described well by linear perturbation of $O(Ca)$ (see Leal 1992) but not beyond.

5.4. *Two-parameter 'steady' shapes*

For $\lambda = 1$, the parameters $\kappa \in (0, 1]$ and $\alpha \in (0, 1)$ in the two-parameter 'steady' shapes (5.4) can be found by minimizing $\|u_n^*\|_S$ with the velocity field $\boldsymbol{u}$ represented by (3.5). Table 3 shows κ and α along with the corresponding error $\|u_n^*\|_S$ for $\lambda = 1$ and various Ca. The error $\|u_n^*\|_S$ is impressively small for the entire range of Ca, but increases significantly as Ca exceeds Ca_{cr} ($Ca = 0.21$ and beyond), where no steady shapes exist, and the resulting dynamics is reflected in ever increasing normal velocity. The values of α again indicate that, for $Ca > 0.1$, the steady shape is no longer close to spheroidal, whereas the values of κ suggest that $Ca_{cr} \sim 0.2$, which is fairly close to Ca_{cr} for pointwise and Chebyshev-series steady shapes.

Figure 8 compares two-parameter 'steady' shapes (solid lines) with the corresponding pointwise steady shapes (dots) and 'steady' spheroids (diamonds) for $\lambda = 1$ and $Ca = 0.1$, 0.15 and 0.196. At $Ca = 0.1$, all three shape approximations coincide. At $Ca = 0.15$, the spheroid slightly deviates from the pointwise shape, whereas the latter and the two-parameter 'steady' shape are visually indistinguishable. At $Ca \sim Ca_{cr}$, the two-parameter 'steady' shape still has a relatively small error, but, being a convex shape by definition, it does not exhibit a minor dimple near the axis of symmetry, shown by the pointwise steady shape.

The approximation (5.4) is a powerful tool for practical use if the dependence of the parameters κ and α on Ca and λ is available. In fact, while in table 3, κ and α follow from direct minimization of $\|u_n^*\|_S$, they can also be determined by fitting the already found pointwise steady shapes with (5.4), which is simply a nonlinear regression. Table 4 presents results of the nonlinear regression, i.e. κ, α and the fitting

https://doi.org/10.1017/jfm.2013.6 Published online by Cambridge University Press

Ca	κ	α	$\|u_n^*\|_S$
0.05	0.745 491	0.499 162	5.3×10^{-5}
0.1	0.563 305	0.487 145	3.4×10^{-3}
0.15	0.394 575	0.418 513	8.3×10^{-3}
0.19	0.226 804	0.241 188	4.1×10^{-4}
0.192	0.217 173	0.229 406	1.0×10^{-3}
0.196	0.197 173	0.204 768	4.1×10^{-3}
0.2	0.176 766	0.180 017	8.2×10^{-3}
0.21	0.131 028	0.129 410	2.5×10^{-2}
0.22	0.121 664	0.134 429	5.3×10^{-2}
0.25	0.147 948	0.286 999	1.2×10^{-1}
0.28	0.128 194	0.419 554	1.6×10^{-1}

TABLE 3. Parameters κ and α in the two-parameter 'steady' shape (5.4) and corresponding kinematic condition error $\|u_n^*\|_S$ for $\lambda = 1$ and various Ca.

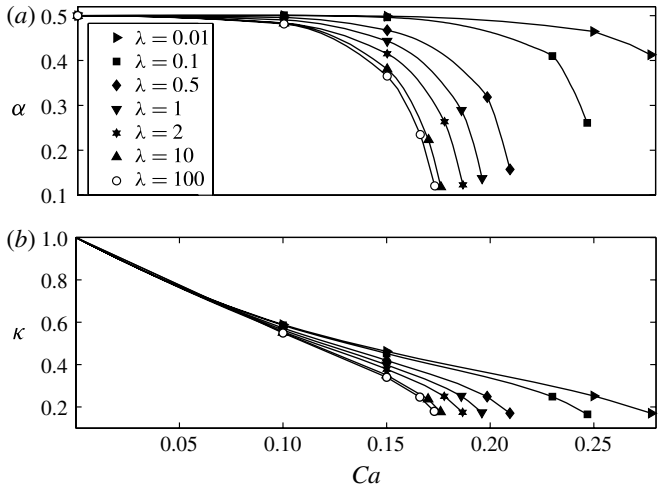


FIGURE 11. Parameters α and κ in (5.4) versus Ca for $\lambda = 0.01$, 0.1, 0.5, 1, 2, 10 and 100.

error for various Ca and λ, whereas figure 11 shows interpolated α and κ within the interval $0 < Ca < Ca_{cr}$ based on the values in table 4 for fixed λ, thereby providing the sought dependence. Now for any given pair Ca and λ, the parameters κ and α in (5.4) can be either taken from figure 11 or re-interpolated from table 4. Note that, in table 3 and in table 4 for $\lambda = 1$, the corresponding α and κ values do not coincide, but are sufficiently close. This is not surprising since the approximated pointwise steady shapes have non-zero error $\|u_n^*\|_S$. Also, each pair of α and κ in table 3 is a minimizer of $\|u_n^*\|_S$, so that, for corresponding Ca and λ, it provides the lowest $\|u_n^*\|_S$ among all pairs of α and κ, in particular those in table 4. This means that as functions of Ca and λ, the parameters α and κ that minimize $\|u_n^*\|_S$ directly will slightly deviate from those shown in figure 11.

For the cases $\lambda = 0.01$ and 0.1, where no dimples appear as $Ca \to Ca_{cr}$ and both the pointwise steady shape and its approximation (5.4) are flat but convex, the deviations

https://doi.org/10.1017/jfm.2013.6 Published online by Cambridge University Press

λ	Ca	κ	α	Fitting error
0.01	0.1000	0.589 016	0.500 133	0.003 734
0.01	0.1500	0.462 418	0.498 615	0.033 549
0.01	0.2500	0.251 810	0.464 622	0.011 039
0.01	0.2777	0.170 700	0.412 698	0.030 108
0.1	0.1000	0.585 682	0.500 932	0.010 973
0.1	0.1500	0.452 588	0.496 079	0.047 667
0.1	0.2300	0.249 006	0.409 995	0.037 763
0.1	0.2469	0.165 556	0.260 922	0.035 560
0.5	0.1000	0.572 771	0.495 759	0.006 250
0.5	0.1500	0.419 905	0.467 517	0.014 870
0.5	0.1985	0.248 994	0.318 423	0.039 868
0.5	0.2095	0.170 463	0.157 421	0.137 386
1	0.1000	0.563 789	0.490 430	0.003 483
1	0.1500	0.398 676	0.443 297	0.018 793
1	0.1860	0.251 584	0.289 139	0.029 045
1	0.1960	0.173 851	0.137 383	0.202 750
2	0.1000	0.555 752	0.483 450	0.016 292
2	0.1500	0.378 443	0.414 947	0.022 144
2	0.1778	0.250 326	0.263 733	0.018 848
2	0.1867	0.174 970	0.122 903	0.256 538
10	0.1000	0.551 868	0.482 925	0.007 085
10	0.1500	0.350 885	0.380 890	0.030 966
10	0.1700	0.237 201	0.223 235	0.017 891
10	0.1760	0.176 715	0.118 090	0.296 950
100	0.1000	0.549 455	0.481 428	0.008 820
100	0.1500	0.340 314	0.365 498	0.031 677
100	0.1660	0.246 804	0.234 988	0.013 802
100	0.1730	0.179 868	0.120 549	0.281 313

TABLE 4. Parameters κ and α and the fitting error (square root of the total quadratic error) from fitting the pointwise steady shapes with the approximation (5.4) for various λ and Ca.

of the two-parameter prediction from the pointwise steady shapes are minute along the entire range of Ca. However, for the cases with $\lambda = O(1)$ or higher, the fitting error is small for all Ca except near the critical capillary numbers, where somewhat larger deviations occur between the convex approximations (5.4) and the concave regions in the pointwise steady shapes. The deviation in these regions is an order of magnitude higher, yet small.

6. Concluding remarks

The deformation of a drop in a linear axisymmetric compressional viscous flow (also known as negative or biaxial extension) was studied, with a particular attention given to a relative low viscosity of the drop. For arbitrary Ca and λ, the problem was solved with an integral equation numerically, whereas for $\lambda = 1$, the velocity field has an exact integral representation and the steady shapes were found in the form of

https://doi.org/10.1017/jfm.2013.6 Published online by Cambridge University Press

Chebyshev series. For spheroidal drops, an analytical solution was obtained with the approach presented in Zabarankin & Nir (2011). Also, a two-parameter approximation for the steady shapes was suggested, and the results obtained with the integral equation approach and via spheroidal and two-parameter shape approximations were analysed and compared one to another.

It was anticipated that, the lower the viscosity of the drop, the more deformed stable stationary shapes at ever increasing capillary numbers could be obtained, as is the case for the deformation of prolate drops embedded in extensional flow. However, contrary to this expectation, it was found rather surprisingly that the extent of deformation at critical Ca (beyond which no stable shapes exist) is very similar for $\lambda = O(1)$ and $\lambda \ll 1$, with the Taylor deformation parameter being $D \sim 0.75$ and with the most deformed drop shape resembling a flat disc with rounded rim. The limited deformation was also reported by Stone & Leal (1989) for the cases $\lambda = 1$ and 10. This pattern is in complete contrast to the ever increasing deformation of such drops in extensional flow (see e.g. Acrivos & Lo 1978).

The spheroidal approximation, given the existence of an analytical solution, requires minimal computational effort (minimizing $\|u_n^*\|_S$ is merely a single-parameter optimization). However, it does not correctly reflect the qualitative form of the steady shapes even for Ca being far from critical values, in which cases it underestimates deformation substantially. Indeed, it was found that only in a region of relatively low capillary input, $Ca \leqslant 0.1$, can the dynamics, the flow field and the ultimate steady shape be obtained analytically rather than resorting to tedious numerical procedures. For comparison, recall that the critical Ca for a steady shape to exist in extensional flow for $\lambda = 1$ is $\sim$0.06 (Rallison & Acrivos 1978; Zabarankin & Nir 2011), which is just about a third of that for the compressional flow. This limited interval of low Ca suggests why spheroidal shapes appear to be much more appropriate approximations for the drop deformation in extensional flow than in compressional flow: the smaller Ca is, the better the true steady shapes agree with the second-order perturbation theory. However, for $\lambda = 0$, the situation is different: for the compressional flow, the critical Ca is finite, $\sim$0.28, whereas for the extensional flow, the slender-body theory (e.g. Acrivos & Lo 1978) shows that the deformation and Ca can grow indefinitely. In other words, the analysis of the difference in critical Ca and D for extensional and compressional flows should also involve λ. This issue deserves further investigation in the broader scope of the stability of the steady shapes.

It should be noted that all the methods used in this paper to solve for the dynamics and the ultimate steady deformation require extra care as the critical capillary number is approached. The iterative procedure for pointwise steady shapes required only 50 surface elements per half a drop length as long as $Ca < Ca_{cr}$. However, in most deformed shapes that showed dimples as $Ca \to Ca_{cr}$, the number was increased to 200. Similarly, Algorithm 1 in Zabarankin & Nir (2011) can make $\|u_n^*\|_S$ for the Chebyshev-series steady shape, with potentially infinite number of series terms, as small as specified, and even with five or six terms, the shape correctly reflects the qualitative form (e.g. a dimple for Ca close to the critical value). However, for a large number of terms, the algorithm becomes computationally expensive, and for Ca close to critical values, it may not converge, regardless of the number of terms. Finally, the two-parameter 'steady' shape has fairly small $\|u_n^*\|_S$ for the whole range of Ca and is computationally inexpensive. However, being convex, it fails to capture dimples of steady shapes for Ca close to critical values despite still providing small $\|u_n^*\|_S$. Hence, the shape that it predicts, with a similar degree of numerical accuracy as given by the pointwise and Chebyshev-series steady shapes, is slightly but qualitatively different.

https://doi.org/10.1017/jfm.2013.6 Published online by Cambridge University Press

Acknowledgements

The authors are grateful to the anonymous referees for their valuable comments and suggestions, which helped to improve the quality of the paper. O.M.L. acknowledges the support of the Israel Ministry of Immigrant Absorption.

REFERENCES

ACRIVOS, A. & LO, T. S. 1978 Deformation and breakup of a single slender drop in an extensional flow. *J. Fluid. Mech.* **86**, 641–672.

ARIS, R. 1962 *Vectors, Tensors and Basic Equations of Fluid Mechanics*. Prentice-Hall.

BARTHÈS-BIESEL, D. & ACRIVOS, A. 1973 Deformation and burst of a liquid droplet freely suspended in a linear shear field. *J. Fluid Mech.* **61**, 1–21.

BAZHLEKOV, I. B., CHESTERS, A. K. & VAN DE VOSSE, F. N. 2000 The effect of the dispersed to continuous-phase viscosity ratio on film drainage between interacting drops. *Intl J. Multiphase Flow* **26**, 445–466.

COX, R. G. 1969 Deformation of a drop in a general time-dependent fluid flow. *J. Fluid Mech.* **37**, 601–623.

DAVIS, R. H. 1999 Buoyancy-driven viscous interaction of a rising drop with a smaller trailing drop. *Phys. Fluids* **11**, 1016–1028.

EGGLETON, C. D. & STEBE, K. J. 1998 An adsorption–desorption-controlled surfactant on a deforming droplet. *J. Colloid Interface Sci.* **208**, 68–80.

FRANKEL, A. N. & ACRIVOS, A. 1970 Constitutive equation for a dilute emulsion. *J. Fluid Mech.* **4**, 65–78.

HAPPEL, J. & BRENNER, H. 1965 *Low Reynolds Number Hydrodynamics*. Nordhoff.

HOBSON, E. W. 1955 *The Theory of Spherical and Ellipsoidal Harmonics*. Chelsea.

HOOPER, R., TOOSE, M., MACOSKO, C. W. & DERBY, J. J. 2001 A comparison of boundary element and finite element methods for modeling axisymmetric polymeric drop deformation. *Intl J. Numer. Meth. Fluids* **37**, 837–864.

KANG, I. S. & LEAL, L. G. 1989 Numerical solution of axisymmetric, unsteady free-boundary problems at finite Reynolds number. II. Deformation of a bubble in a biaxial straining flow. *Phys. Fluids* A **1**, 644–660.

LAC, E. & HOMSY, G. M. 2007 Axisymmetric deformation and stability of a viscous drop in a steady electric field. *J. Fluid Mech.* **590**, 239–264.

LADYZHENSKAYA, O. A. 1969 *The Mathematical Theory of Viscous Incompressible Flow*. Gordon and Breach.

LAVRENTEVA, O. M., BEREZHNOV, V. & NIR, A. 2002 Axisymmetric motion of a pair of deformable heavy drops in an upward temperature gradient. *Phys. Fluids* **14**, 1326–1339.

LEAL, L. G. 1992 *Laminar Flow and Convective Transport Processes*. Butterworth-Heinemann.

LEVICH, V. G. 1962 *Physicochemical Hydrodynamics*. Prentice-Hall.

NAVOT, Y. 1999 Critical behavior of drop breakup in axisymmetric viscous flow. *Phys. Fluids* **11**, 990–996.

PAYNE, L. E. & PELL, W. H. 1960 The Stokes flow problem for a class of axially symmetric bodies. *J. Fluid Mech.* **7**, 529–549.

POZRIKIDIS, C. 1992 *Boundary Integral and Singularity Methods for Linearized Viscous Flow*. Cambridge University Press.

RALLISON, J. M. & ACRIVOS, A. 1978 A numerical study of the deformation and burst of a viscous drop in an extensional flow. *J. Fluid Mech.* **89**, 191–200.

SMAGIN, I., PATHAK, M., LAVRENTEVA, O. M. & NIR, A. 2011 Motion and shape of an axisymmetric viscoplastic drop slowly falling through a viscous fluid. *Rheol. Acta* **50**, 361–374.

STONE, H. A. 1994 Dynamics of drop deformation and breakup in viscous flow. *Annu. Rev. Fluid Mech.* **26**, 65–102.

STONE, H. A. & LEAL, L. G. 1989 A note concerning drop deformation and breakup in biaxial extensional flows at low Reynolds numbers. *J. Colloid Interface Sci.* **133**, 340–347.

https://doi.org/10.1017/jfm.2013.6 Published online by Cambridge University Press

TAYLOR, G. I. 1934 The formation of emulsions in definable fields of flow. *Proc. R. Soc.* A **146**, 501–523.

TOOSE, E. M., VAN DEN ENDE, D., GEURTS, B. J., KUERTEN, J. G. M. & ZANDBERGEN, P. J. 1996 Axisymmetric non-Newtonian drops treated with a boundary integral method. *J. Engng Maths* **30**, 131–150.

VLAHOVSKA, P. M., LOEWENBERG, M. & BLAWZDZIEWICZ, J. 2005 Deformation of a surfactant-covered drop in a linear flow. *Phys. Fluids* **17**, 103103.

ZABARANKIN, M. 2008 The framework of *k*-harmonically analytic functions for three-dimensional Stokes flow problems, Part I. *SIAM J. Appl. Maths* **69**, 845–880.

ZABARANKIN, M. & MOLYBOHA, A. 2011 3D shape optimization in viscous incompressible fluid under Oseen approximation. *SIAM J. Control Optim.* **49**, 1358–1382.

ZABARANKIN, M. & NIR, A. 2011 Generalized analytic functions in an extensional Stokes flow with a deformable drop. *SIAM J. Appl. Maths* **71**, 925–951.

https://doi.org/10.1017/jfm.2013.6 Published online by Cambridge University Press